Polypyrrole-reduced graphene oxide coated delignified wood for highly efficient solar interfacial steam generation

Wong, M. Y.; Zhu, Y.; Ho, T. C.; Pan, A.; Tso, C. Y.

Published in:
Applied Thermal Engineering

Published: 25/01/2023

Document Version:
Post-print, also known as Accepted Author Manuscript, Peer-reviewed or Author Final version

Published version (DOI):
10.1016/j.applthermaleng.2022.119686

Publication details:
Wong, M. Y., Zhu, Y., Ho, T. C., Pan, A., & Tso, C. Y. (2023). Polypyrrole-reduced graphene oxide coated delignified wood for highly efficient solar interfacial steam generation. *Applied Thermal Engineering*, *219*(Part D), Article 119686. https://doi.org/10.1016/j.applthermaleng.2022.119686

Polypyrrole-Reduced Graphene Oxide Coated Delignified Wood for Highly Efficient Solar Interfacial Steam Generation

M.Y. Wong[1], Y. Zhu[1], T.C. Ho[1], A. Pan[1], C.Y. Tso[1,*]

[1] School of Energy and Environment, City University of Hong Kong, Hong Kong

* Corresponding Author Tel.: +852 3442 4623

E-mail address: chiytso@cityu.edu.hk

Address: School of Energy and Environment, City University of Hong Kong, Tat Chee Avenue, Kowloon, Hong Kong

Keywords: Evaporation, Solar Absorption, Photothermal Conversion, Heat Transfer, Solar-to-Vapor Conversion Efficiency

Abstract

A solar interfacial steam generator is a device that localizes the solar energy at the water-air interface for water evaporation. The solar interfacial steam generator can be applied in various evaporation-based thermal systems to enhance system efficiency by reducing heat dissipation. In this study, a bio-inspired polypyrrole-reduced graphene oxide coated wood was fabricated and investigated for evaporation and solar-to-vapor conversion efficiency improvement with different polypyrrole-reduced graphene oxide ratios. Thanks to the synergistic effect of highly solar-absorbed polypyrrole and water-attracted reduced graphene oxide, and the efficient heat transfer two-dimensional pathway, the polypyrrole-reduced graphene oxide coated wood showed an outstanding water evaporation performance. The highest water evaporation rate obtained by the polypyrrole-reduced graphene oxide coated wood with the reduced graphene oxide content of 60% was 1.49 $kg \cdot m^{-2} \cdot hr^{-1}$, showing a nearly 10% and 19% improvement compared to polypyrrole and reduced graphene oxide coated woods, respectively. The corresponding solar-to-vapor conversion efficiency (93.1%) was also beyond most of the wood-based interfacial steam generators in the literature. The transient heat transfer and evaporation performances of the polypyrrole-reduced graphene oxide coated wood were also firstly investigated based on the developed transient models. It is expected that the remarkable

results of this study can help to promote and facilitate the study and application of interfacial steam generators in various thermal systems.

Graphical Abstract

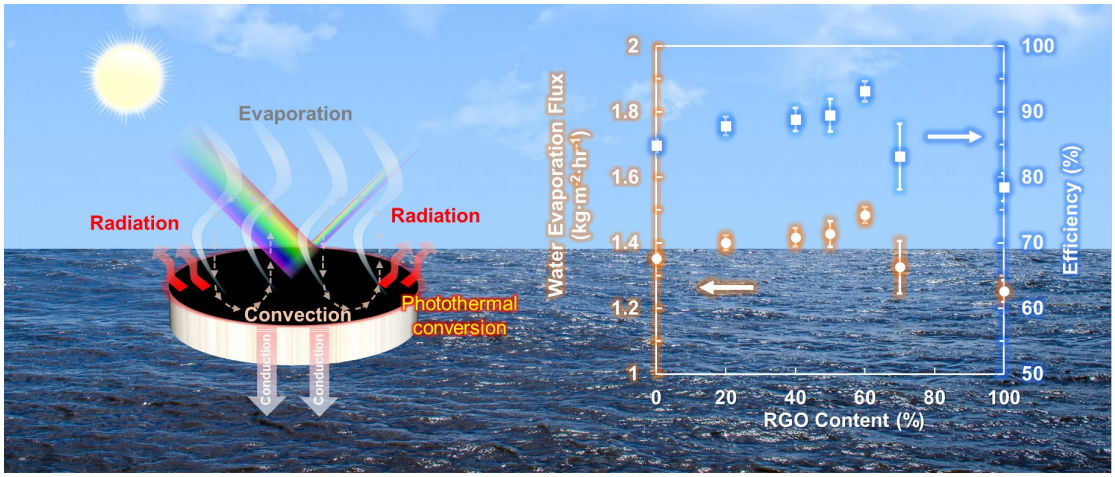

Nomenclature

A	Coefficient [-]
A_s	Surface area [m^2]
B	Coefficient [-]
C_{opt}	Optical concentration factor [-]
c_p	Specific heat capacity [$J \cdot kg^{-1} \cdot K^{-1}$]
k	Thermal conductivity [$W \cdot m^{-1} \cdot K^{-1}$]
h	Heat transfer coefficient [$W \cdot m^{-2} \cdot K^{-1}$]
h_{fg}	Latent heat of water [$J \cdot kg^{-1}$]
l	Thickness [m]
$\dot{m}_e$	Water evaporation flux [$kg \cdot m^{-2} \cdot hr^{-1}$]
Δm_w	Water weight loss [g]
n	Coefficient [-]
P	Pressure [Pa]
P_0	Solar intensity [$W \cdot m^{-2}$]
q	Heat flux [$W \cdot m^{-2}$]
SSE	Sum of squared estimate error [-]
T	Temperature [K]
t	Time interval [s]

Δt	Duration [s]
T_0	Ambient temperature [K]
V	Volume [m^3]
$y_{e,i}$	Measured value of the water evaporation rate [-]
$y_{p,i}$	Predicted value of the water evaporation rate [-]

Greek letter

α	Solar absorptance [-]
δ	Uncertainty [-]
ε	Optical emittance [-]
η_e	Solar-to-vapor conversion efficiency [%]
θ	Angle [°]
ν	Wind velocity [$m \cdot s^{-1}$]
ρ	Density [$kg \cdot m^{-3}$]
σ	Stefan-Boltzmann constant (5.67×10^{-8} $W \cdot m^{-2} \cdot K^{-4}$)
φ	Relative humidity [-]
ϕ	Porosity [-]

Subscript

a	Air
cond	Conduction
conv	Convection
drywood	Wood in the dry state
evap	Evaporation
rad	Radiation
solar	Solar radiation
w	Water surface
wood	Wood

1. Introduction

Solar-driven water evaporation is an essential part of the natural water cycle. The evaporation process not only generates steam or vapor but also helps to separate the impurities from water. As a result, the solar-driven water evaporation process is utilized in various applications, such

as seawater desalination [1], wastewater purification [2], sterilization [3], and power generation [4]. To improve solar evaporation efficiency, several heating approaches, such as bottom heating, volumetric heating, and interfacial heating, have been proposed and investigated in the literature [5]. Among them, the interfacial heating approach, which is the emerging evaporation approach, has the shortest response time with a high potential to break the current solar-driven water evaporation limit [5–7].

The interfacial heating approach localizes the solar energy near the water-air interface, minimizing heat dissipation. A typical two-dimensional interfacial steam generator consists of a solar absorbing surface and a substrate for water supply, thermal insulation, and floating in water [8]. The performance of the interfacial steam generator can be evaluated by the solar-to-vapor conversion efficiency (as shown in Equation (1)), which is determined by the ratio of the energy converted into the latent heat of water evaporation and the incoming solar energy. The solar-to-vapor conversion efficiency of the interfacial steam generator can be improved by using high solar absorption and photothermal conversion coating materials for the solar absorbing surface. Besides, minimizing the conductive, convective, and radiative heat loss and providing sufficient water supply can enhance the solar-to-vapor conversion efficiency of the interfacial steam generator.

$$\eta_e = \frac{\dot{m}_e h_{fg}}{C_{opt} P_0}, \tag{1}$$

where $\dot{m}_e$ is the water evaporation flux ($kg \cdot m^{-2} \cdot s^{-1}$), h_{fg} is the latent heat ($J \cdot kg^{-1}$) of water, C_{opt} is the optical concentration factor of the solar input, and P_0 is the solar intensity ($W \cdot m^{-2}$).

Inspired by the transpiration in plants, where the wood structure guarantees continuous water supply from underground to the leaf through the capillary effect and the difference in water potential, wood-based interfacial steam generators were proposed and investigated in the literature [9–19]. There are many advantages to use wood as the substrate of an interfacial steam generator, namely low density, high thermal resistance, hydrophilic nature, and high mechanical strength [20]. Besides, the 3D microchannels of wood can further improve solar absorption through light scattering and facilitate the water and vapor flow through the capillary effect. Compared to synthesised materials with tuneable structures, wood structure is more stable in terms of mechanical structure and thermophysical properties, and durable thanks to

the results of a million-year evolution [21]. The complexity of the synthesised material fabrication process may also cause defects in the materials, influencing their function. Moreover, wood is a sustainable and bio-degradable material. As a result, the environmental pollution caused by the application of wood-based interfacial steam generators can be minimized at different stages of their lifetime (i.e. fabrication, application, and disposal).

On the other hand, the solar absorbing surface of the interfacial steam generator is composed of photothermal materials which can convert light into thermal energy, via plasmonic heating, non-radiative relaxation, and molecular thermal vibration, depending on the material properties [22–24]. The photothermal materials used in interfacial steam generators can be categorized into metal (gold, silver), metal oxides, semiconductors (Cu_7S_4, TiO_2, Fe_3O_4), and organic materials (carbon, graphene, carbon nanotube) [23]. Among them, carbon-based photothermal materials attracted lots of attention because of their low cost, easy fabrication, solar broadband absorption performance, high photothermal conversion ability, and reusability [25]. Reduced graphene oxide (RGO) is a promising material for solar interfacial steam generation because of its large two-dimensional surface area, low density, low specific heat capacity, high thermal conductivity, and high solar broadband absorption [25–27]. However, it should be noted that RGO layers tend to restack together as graphite powder because of the strong $\pi - \pi$ interaction between RGO layers [28]. The restacking of RGO layers not only significantly reduces the surface area of the RGO for water evaporation and solar absorption, but also resists the heat transfer among RGO. Fabricating three-dimensional (3D) structured RGO materials through freeze-drying can relieve the restacking effect because the interlocked and interconnected 3D structure can resist agglomeration of the RGO layers [28]. Forming RGO composite materials can also alleviate the restacking effect. The $\pi - \pi$ interaction or hydrogen bonding between RGO and polymers or other carbon materials can weaken the interaction between RGO layers, relieving the self-stacking effect of RGO [28, 29]. Polypyrrole (PPY) is a conjugated polymer composed of carbon and nitrogen atoms. It is widely used in various interfacial steam generators as a solar absorption material due to its high solar absorption ability and photothermal performances [10, 30–33]. The solar absorption of the PPY coated wood can be up to 98% according to the literature [9, 10]. Apart from preventing restacking of the RGO layer, it is claimed that the 2D network of the RGO can also help to improve the energy transfer between the PPY nanoparticles [34]. Therefore, it is expected that combining PPY and RGO can result in a solar absorption layer with improved solar absorption performance and enhanced

thermal transport. It should be pointed out that there is no study on the PPY-RGO composite of a wood-based interfacial steam generator in the literature to date.

Therefore, this study aims to investigate the photothermal and water evaporation performances of the PPY-RGO coated wood with various PPY-RGO ratios. Besides, the photothermal and water evaporation enhancement and the underlying mechanisms of the PPY-RGO coated wood compared to pure PPY and RGO coated wood have been studied numerically and experimentally. Most importantly, for the first time, mathematical models were developed to comprehensively investigate the transient heat transfer and evaporation behaviors of the PPY-RGO coated wood during evaporation for the application of solar interfacial steam generation.

2. Experiment

In this section, the synthesis of PPY, RGO, and PPY-RGO composite materials, and the fabrication of the PPY-RGO coated woods are presented. Then, the characterization of the PPY-RGO composites and the PPY-RGO coated woods is illustrated. Next, the experimental setup of the water evaporation tests for the PPY-RGO coated woods is described. The experimental uncertainties are also analyzed at the end of this section.

2.1. Material preparation

The PPY-RGO composite powder was fabricated according to Bose et al. [35]. However, it should be noted that the PPY-RGO composite powder was utilized as a supercapacitor in the previous study [35]. Therefore, there is an unknown in the photothermal and evaporation enhancement of the PPY-RGO composite powder in this study. Pyrrole, iron (III) chloride ($FeCl_3$), natural graphite flakes (~325 mesh particle size), 95.0 – 98.0% sulfuric acid (H_2SO_4), potassium permanganate ($KMnO_4$), 30% hydrogen peroxide (H_2O_2), 10% hydrochloric acid (HCl), hydrazine monohydrate (NH_2NH_2 in water), absolute ethanol, sodium chlorite ($NaClO_2$), and 99% acetic acid, were purchased from Sigma Aldrich and directly used in the synthesis.

2.2. Polypyrrole (PPY) synthesis

The polymerization process was activated by adding 50 ml of 0.1 M $FeCl_3$ solution into a 0.5 M pyrrole DI water-ethanol solution (DI water: ethanol = 50:50) with the same volume (as shown in Figure 1 (a)). The color change of the mixture from transparent to black indicated the activation of the polymerization process. After stirring for 24 hours at room temperature, the

mixture was filtered and washed with DI water and ethanol to remove the residual $FeCl_3$. The obtained PPY powder was dried at 60 ºC for 24 hours before it was ready to use.

2.3. Reduced graphene oxide (RGO) synthesis

RGO was synthesized by oxidizing graphite into graphene oxide by the modified Hummers method [36], followed by chemical reduction of the graphene oxide, as shown in Figure 1 (a). A mixture of 2 g of graphite flakes and 46 ml of H_2SO_4 was stirred for 30 minutes in an ice bath. Then, 6 g of $KMnO_4$ was gently added to the mixture for one hour while maintaining the temperature of the mixture below 20 ºC. After one hour of stirring at room temperature, the mixture was stirred for another hour under 35 ºC. Then, 100 ml of DI water was added dropwise into the mixture for oxidation while maintaining the temperature of the mixture below 80 ºC. Next, the temperature of the mixture was maintained at 80 ºC for 30 minutes. After adding 200 ml of DI water and stirring for 30 minutes without further heating, the oxidation process was terminated by introducing 5 ml of 30% H_2O_2 into the mixture. The color of the mixture turned golden yellow. The mixture was centrifuged several times while being washed with 5% of HCl solution and DI water to remove the acidic residue. The graphene oxide powder was obtained after freeze-drying. Afterward, the reduction process of graphene oxide powder was performed. 0.1 g of graphene oxide powder was dissolved into 50 ml of DI water. The solution underwent ultrasonic treatment for 30 minutes to ensure equal distribution. Then, 1 ml of hydrazine monohydrate was added to the solution. The solution was heated to 95 ºC for 6 hours for the reduction. After filtering and washing with DI water, the reduced graphene oxide (RGO) powder was finally dried at 60 ºC for 24 hours.

2.4. PPY-RGO composite synthesis

Seven weight ratios of PPY-RGO composite were investigated in this study, namely 100:0 (PPY), 80:20 (P80G20), 60:40 (P60G40), 50:50 (P50G50), 40:60 (P40G60), 20:80 (P20G80), and 0:100 (RGO). Firstly, 0.2 M PPY powder was dispersed in a 30 ml DI water-ethanol solution (50:50). Simultaneously, GO powder was added to 50 ml DI water. The two solutions were placed into separate ultrasonic baths for 30 minutes. Then, the PPY solution was added to the GO solution. Another 30-minute ultrasonication was performed to ensure the uniformity of the PPY-GO solution. Next, 20 ml of 0.1 M $FeCl_3$ solution was added to the PPY-GO solution to start the polymerization process which lasted for 24 hours under stirring. Then, the solution was filtered and washed with DI water and ethanol. After drying at 60 ºC for 24 hours, PPY-GO composite was obtained. The reduction process was performed to transform the PPY-

GO composite into a PPY-RGO composite. The reduction process was identical to the reduction process of GO powder, as shown in Figure 1 (a).

2.5. PPY-RGO coated wood fabrication

Balsa wood was used in this study as it is one of the fasting growing wood species in the world. Therefore, the sustainable supply of raw Balsa wood can be guaranteed. The fast growth of balsa wood also leads to low density (high porosity) [37]. A previous study indicated that the evaporation performance of the wood-based interfacial steam generator can be improved while using the wood species with a higher porosity [12]. As a result, balsa wood with high porosity (90% [12]) is a suitable material for the substrate. Balsa wood of 4 cm in diameter and 1.5 cm thick was prepared for this study. Before coating the PPY-RGO composite on the wood surface, the wood block underwent a delignification process to remove the lignin. Therefore, the thermal insulation and water transport performance of the wood block can be improved [38]. A 200 ml of 0.4 M sodium chlorite solution was first prepared. Then, acetic acid was added to the solution to reduce the pH value to around 4.6. After placing the wood block into the solution, the solution was heated to 80 ºC for 6 hours. The delignified wood was then washed with DI water several times and dried at 60 ºC for 24 hours. To coat the PPY-RGO composite on the wood surface, the delignified wood block was heated to 90 ºC. Next, the wood was drop-coated in 3 ml of 1% ethanol-based PPY-RGO composite nanofluid. The coated wood sample was ready for the water evaporation test after drying at 70 ºC for 24 hours. The whole fabrication and the photos of PPY-RGO coated wood are shown in Figure 1(a).

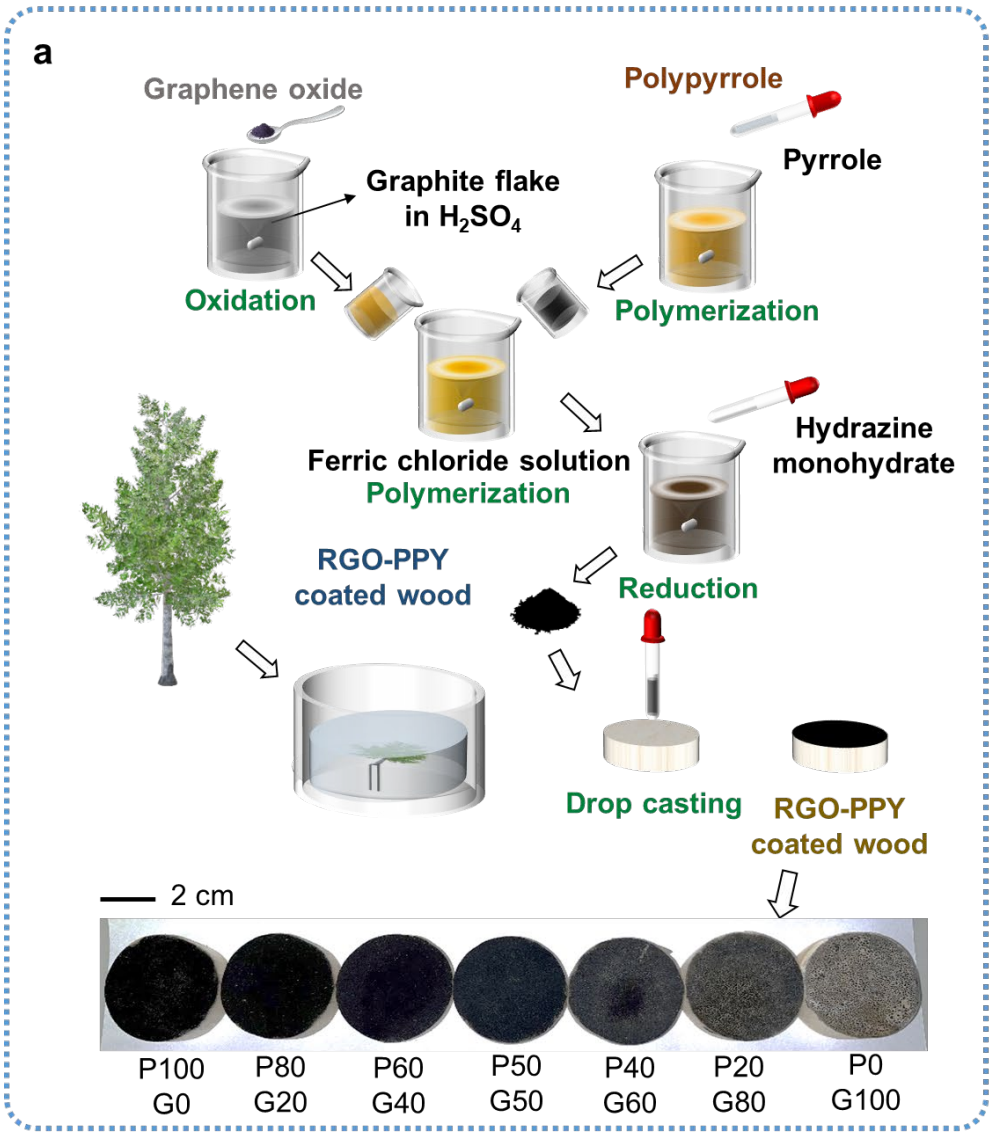
a
Graphene oxide
Graphite flake in H_2SO_4
Oxidation
Polypyrrole
Pyrrole
Polymerization
Ferric chloride solution
Polymerization
Hydrazine monohydrate
RGO-PPY coated wood
Reduction
Drop casting
RGO-PPY coated wood
2 cm
P100 G0
P80 G20
P60 G40
P50 G50
P40 G60
P20 G80
P0 G100

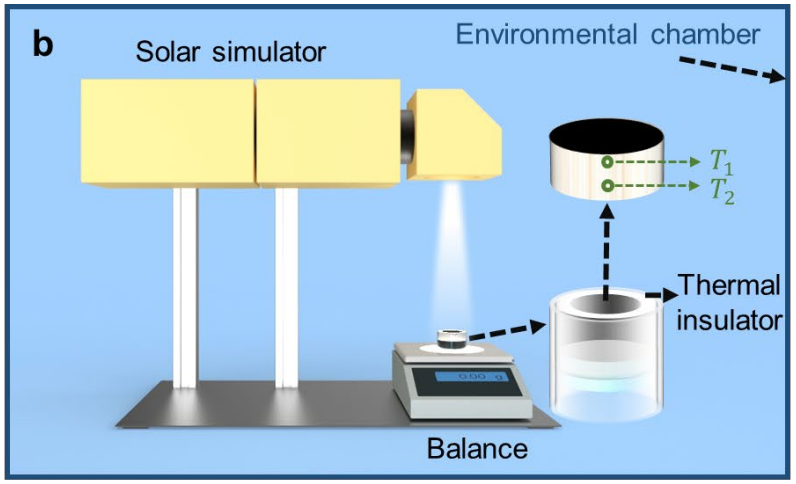
b
Solar simulator
Environmental chamber
T_1
T_2
Thermal insulator
Balance

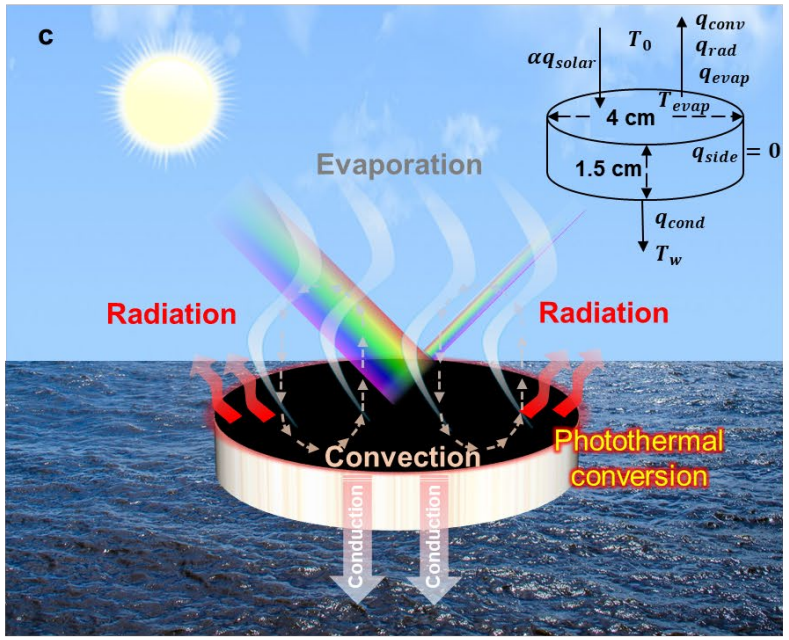
c
αq_{solar}
T_0
q_{conv}
q_{rad}
q_{evap}
T_{evap}
4 cm
1.5 cm
$q_{side} = 0$
q_{cond}
T_w
Evaporation
Radiation
Radiation
Convection
Photothermal conversion
Conduction
Conduction

Figure 1: (a) Fabrication process and photos of the PPY-RGO coated woods. (b) Experimental setup of the water evaporation test. (c) Heat transfer diagram of the interfacial steam generator.

2.6. Sample characterization

First, the elemental identification was conducted using X-ray diffraction (XRD) analysis (X'Pert^3 Power, Malvern Panalytical) from $2\theta = 10°$ to $2\theta = 100°$, then the optical absorptance spectrum from UV-VIS-NIR spectrometer (Lambda 1050+, PerkinElmer) in the range of 200 – 800 nm. PPY-RGO composite materials in powder form were used in the XRD analysis. The light absorptance of the 0.01 wt% PPY-RGO nanofluids was utilized for the elemental identification. PPY-RGO coated wood samples were used in the UV-VIS-NIR spectrometer for solar absorption performance evaluation. The surface morphology of the PPY-RGO coated woods was observed using scanning electron microscopy (SEM) (EVO MA 10, ZWISS) with an acceleration voltage of 10-15 kV. The photothermal performance of the PPY-RGO coated woods was investigated by recording the temperature change of the coated woods under the illumination of the solar simulator (SciSun-300, Sciencetech) for 30 minutes. The temperature of the coated wood was measured by one thermocouple attached to the coated wood in the T_1 position as indicated in Figure 1(b). Thermal images of the coated wood were also taken using a thermal infrared camera (E75, FLIR) at the end of each test.

2.7. Experimental setup for water evaporation tests

The water evaporation performance of the PPY-RGO coated wood was evaluated inside an environmental chamber (27 ^oC, 50% RH) (TH-TG-300, Jeio tech). Figure 1(b) shows the solar steam generation experimental setup for the water evaporation rate measurement. A glass container with 15 ml of DI water was placed on an electronic balance. A solar simulator (SciSun-300, Sciencetech) attached with an optical filter for the standard AM 1.5G spectrum was placed on top of the glass container to provide artificial sunlight with an intensity of 1000 $W{\cdot}m^{-2}$. The readings of the electronic balance were recorded by computer software. Two K-type thermocouples were inserted into the samples as shown in Figure 1(b) to measure the temperature profiles of the sample during the evaporation process. Thermal images of the samples were also taken using a thermal infrared camera (E75, FLIR). Before the experiment, a PPY-RGO coated wood was placed on the water surface of the glass container. After initiating the solar simulator and ensuring the output light intensity reached 1000 $W{\cdot}m^{-2}$, the reading of the electronic balance was set to 0 and the water evaporation test of the sample commenced.

The experiment lasted 1.5 hours to ensure the steady state of water evaporation performance of the samples. The water evaporation flux can be determined by

$$\dot{m}_e = \frac{\Delta m_w}{A_s \Delta t}, \quad (2)$$

where Δm_w is the water weight loss (kg) during the evaporation process, A_s is the surface area (m^2) of the interfacial steam generator sample, and Δt is the duration (s) of the evaporation process. After obtaining the water evaporation flux of the interfacial steam generator, the solar-to-vapor conversion efficiency can be calculated by Equation (1).

2.8. Uncertainty analysis

The uncertainties of the measured water evaporation rates were mainly caused by the weight balance (±0.005 g), timer (±15 s), and human measurement error (±0.5 mm). Based on the error propagation calculation [39], the estimated uncertainty of the water evaporation rate is about 2.55% based on Equation (3).

$$\delta_{\dot{m}_e} = \pm\sqrt{\left(\delta_{\Delta m_w}\right)^2 + \left(\delta_{A_s}\right)^2 + (\delta_{\Delta t})^2}, \quad (3)$$

where $\delta_{\Delta m_w}$, δ_{A_s} and $\delta_{\Delta t}$ are the uncertainties of the water weight loss, evaporation surface area, and the duration of the evaporation process, respectively.

3. Transient Heat Transfer and Evaporation Model Development

Although mathematical heat transfer analysis on the interfacial steam generator is common in the literature, most of the analyses are conducted under steady-state conditions. The transient heat transfer and evaporation performance analysis on the interfacial steam generator is seriously lacking in the literature. Therefore, to gain a deeper understanding of the transient heat transfer mechanisms of the PPY-RGO coated wood, for the first time, mathematical models are developed. As mentioned above, the interfacial steam generator proposed in this work consists of two parts, the solar absorption layer, and the substrate. The solar absorption layer absorbs the incoming solar radiation and converts it into thermal energy to heat water. The substrate continuously transports the water from the water source to the solar absorption

layer to sustain the water evaporation. At the same time, the substrate prevents direct contact between the solar absorption layer and the water source to reduce heat loss. Figure 1(c) shows the heat transfer diagram of the interfacial steam generator. Solar energy is the only energy source for the system. The absorbed solar energy of the system depends on the solar absorptance of the interfacial steam generator surface. The heat loss of the system consists of downward conductive heat loss, and upward convective and radiative heat losses. Several assumptions were adopted in the model: (1) The system is well-insulated at the side and bottom. Therefore, the side heat loss and the water heat loss can be neglected; (2) One-dimensional heat transfer is dominant due to the large aspect ratio (the diameter of the wood is larger than the thickness of the wood) and the insulated side wall; (3) Water transport in the wood is sufficient so that no area dries out on the wood surface during the experiment; (4) The thermal emissivity and the solar absorptance of the wood samples are the same; (5) The convective heat transfer coefficient of the wood surface is temperature-independent; (6) The thermal conductivity of the wood samples do not change with the temperature. The energy for the water evaporation is calculated by subtracting the heat loss from the absorbed solar energy. Based on the diagram (Figure 1(c)), the energy balance equation of the interfacial steam generator can be obtained by

$$\rho_{wood} V_{wood} c_{p,wood} \frac{dT_{wood}}{dt} = \alpha q_{solar} - q_{evap} - q_{conv} - q_{cond} - q_{rad}, \quad (4)$$

$$c_{p,wood} = \phi c_{p,w} + (1-\phi) c_{p,drywood}, \quad (5)$$

where ρ_{wood}, V_{wood} and $c_{p,wood}$ are the density ($kg \cdot m^{-3}$), volume (m^3), and specific heat capacity ($J \cdot kg^{-1} \cdot K^{-1}$) of the sample, respectively, T_{wood} is the temperature (K) of the sample, t is the time interval (s), α is the solar absorptance of the solar absorption layer, q_{solar} is the incoming solar radiation ($W \cdot m^{-2}$), q_{evap} is the water evaporation heat loss ($W \cdot m^{-2}$), and q_{conv}, q_{cond}, q_{rad} are the heat losses ($W \cdot m^{-2}$) from thermal convection, conduction, and radiation, respectively. The specific heat capacity of the sample can be determined by the Maxwell model, where ϕ, and $c_{p,w}$ and $c_{p,drywood}$ are the wood porosity, and the specific heat capacities ($J \cdot kg^{-1} \cdot K^{-1}$) of water and the dry wood, respectively. Since the heat capacity of the PPY-RGO coated layer is nearly 1000 times lower than that of the wood substrate, the heat capacity of the PPY-RGO coated layer is neglected in Equation (5). The calculations of each heat loss are presented as follows.

Firstly, it should be noted that water evaporation is a heat and mass transfer process. To determine the evaporation heat loss, the water evaporation rate has to be determined. There are many empirical correlations presented in the literature to evaluate the water evaporation rate, in the form of Equation (6) [40–42]. The water evaporation process depends on the vapor pressure difference between the saturated water surface and the surrounding air at the dew point. The coefficients A and B are the multiple parameters that are affected by evaporation surface structure and the experimental conditions. It is assumed that a layer of vapor is accumulated near the evaporation surface during evaporation. The accumulated vapor layer will resist the water evaporation. However, due to buoyancy-driven natural air convection or forced convection (wind), the saturated air near the water surface can be replaced by dry air [42]. Since the wind can improve the water evaporation rate, the wind velocity, v, is also considered in the model. Nevertheless, in this work, no additional airflow was introduced during the experiment. As a result, the wind velocity was equal to zero. Moreover, previous studies indicated that the water evaporation rate does not necessarily have a linear relationship with the vapor pressure difference [41]. Thus, a power of n is added to the equation.

$$q_{evap} = h_{evap}(T_{evap} - T_0) = \dot{m}_e h_{fg}, \tag{6}$$

$$\dot{m}_e = (A + Bv)(P_w - \varphi P_a)^n, \tag{7}$$

where h_{evap} is the evaporation heat transfer coefficient ($W \cdot m^{-2} \cdot K^{-1}$), T_{evap} and T_0 are the evaporation surface (wood top surface) and ambient temperatures (K), respectively, P_w and P_a are the vapor pressure at the water surface and surrounding air, respectively, v and φ are the wind velocity ($m \cdot s^{-1}$) and relative humidity, respectively, and A, B, and n are the empirical coefficients. As mentioned, the wind effect was not investigated in the current study. Thus, the coefficient B could be omitted. The coefficient A for different PPY-RGO coated woods could be determined by minimizing the sum of squared estimate errors (*SSE*) under a fixed value of n,

$$SSE = \sum_i (y_{e,i} - y_{p,i})^2, \tag{8}$$

where $y_{e,i}$ and $y_{p,i}$ are measured and predicted water evaporation rates, respectively.

As the surface temperature of the interfacial steam generator is higher than the surrounding environment, the evaporation surface can heat the air near the surface. Due to the density difference, the hot light air near the surface flows up, and the cold air flows down to fill in the air gap. During air circulation, heat is dissipated from the evaporation surface. The convection heat loss, q_{conv}, caused by the air movement can be illustrated by the Nusselt theory [43],

$$q_{conv} = h_{conv}(T_{evap} - T_0), \tag{9}$$

where h_{conv} is the convective heat transfer coefficient ($W \cdot m^{-2} \cdot K^{-1}$). The convective heat transfer coefficient is assumed to be 10 $W \cdot m^{-2} \cdot K^{-1}$ for interfacial steam generation from the literature [44].

The conductive heat loss, q_{cond}, in this study only focuses on the heat transfer from the wood to the water source in the downward direction because the conductive heat loss in the horizontal direction can be neglected [45]. From the literature, the thermal insulation requirement of the interfacial steam generator is less compared to the volumetric heating approach [45]. The conductive heat loss can be determined by Fourier's Law [46], and it can be expressed as,

$$q_{cond} = k_{wood} \frac{\Delta T_{wood}}{l_{wood}}, \tag{10}$$

where k_{wood} is the thermal conductivity ($W \cdot m^{-1} \cdot K^{-1}$) of the saturated wood, $A_{s,wood}$ and l_{wood} are the cross-sectional area (m^2) and thickness (m) of the wood, respectively, and ΔT_{wood} is the temperature difference (K) across the wood.

Finally, the radiative heat loss, q_{rad}, can be determined by the Stefan-Boltzmann Law [47] which can be represented as

$$q_{rad} = \varepsilon\sigma(T_{evap}^4 - T_0^4), \tag{11}$$

where ε is the optical emittance of the solar absorbing surface, and σ is the Stefan-Boltzmann constant (5.67×10^{-8} $W \cdot m^{-2} \cdot K^{-4}$). After determining the evaporation rate of the coated wood by Equation (7) by the best-fit approach, Equations (4) – (6) and (9) – (11) can be solved analytically by inputting the parameters in Table 1. The modeling result can be verified by

comparing the experimental evaporation rate at a particular time and an evaporation surface temperature.

Table 1: Parameters used in the model

Parameters	Values	Parameters	Values
d_{wood}	0.04 m^2	h_{fg}	2,257,000 $J \cdot kg^{-1}$
l_{wood}	0.015 m^2	σ	5.67 $\times 10^{-8}$ $W \cdot m^{-2} \cdot K^{-4}$
k_{wood}	0.0523 $W \cdot m^{-1} \cdot K^{-1}$	h_{conv}	10 $W \cdot m^{-2} \cdot K^{-1}$
q_{solar}	1,000 $W \cdot m^{-2}$	ϕ	0.9
T_0	25 °C	$c_{p,w}$	4,200 $J \cdot kg^{-1} \cdot K^{-1}$
φ	50%	$c_{p,drywood}$	2,900 $J \cdot kg^{-1} \cdot K^{-1}$
n	0.7		

4. Results and Discussion

In this section, the optical properties, surface profiles, and thermal properties of the PPY-RGO coated woods are firstly presented. Then, the water evaporation performance and the underlying mechanisms are illustrated and discussed.

4.1. Optical property

The optical properties of the PPY-RGO composite, PPY, and RGO materials were measured by UV-VIS-NIR spectrometer (UV-3600, Shimadzu) using 0.01 wt% nanofluids. Before measurement, the liquid samples were placed in an ultrasonic bath for one hour to ensure uniformity. The results shown in Figure 2(a) indicate the absorption peak of the RGO is located at 275 nm, which is similar to the literature [48]. There is a local absorption minimum peak at nearly 250 nm and a local absorption maximum peak at 500 nm for PPY, indicating the visible and near-infrared absorption of the PPY. The absorption peaks of the PPY-RGO composites are close to that of PPY and RGO, representing the composition of PPY and RGO. The XRD spectrums of the PPY, RGO, and PPY-RGO composite materials are shown in Figure 2(b). PPY exhibits a broad peak at $2\theta = 25.24°$, representing the amorphous state of PPY. For RGO, the peak of 24° indicates the distances between graphene layers while the peak of 43.1° presents the short-range order in the graphene layers. The PPY-RGO composite materials also exhibit peaks as the combination of PPY and RGO spectra. This indicates the success of composite material fabrication.

The solar absorption performances of different coated wood were measured by the UV-VIS-NIR spectrometer (Figure 2(c)) in the range of 200 nm – 2500 nm. It is noted that the solar absorptance of wood is significantly improved after coating. Among the coated wood, RGO coated wood has the lowest solar absorption performance (88.4%). On the other hand, the solar absorptance of PPY coated wood reaches 98%. The solar absorptance of the PPY and RGO coated wood is similar to the literature [10, 25]. As expected, the higher the PPY content, the higher the solar absorptance of the coated wood because of the supreme solar absorption performance of PPY. Besides, when looking at the photos in Figure 1(a), the restacking effect of RGO was observed when the RGO content is increased. Therefore, the cracking of the coating increased the area of the original wood surface, causing the reduction of the coating area. The solar absorption of the coated wood is thus reduced. Although the reduced solar absorption of the PPY-RGO coated wood leads to a decreased solar input to the samples according to Equation (4), it should be noted that the solar-to-vapor conversion efficiency of the coated wood can also be affected by many other factors, such as the photothermal conversion efficiency of the coating, and the heat transfer between the coating and the water molecules. Therefore, more measurements were conducted and discussed in the following section to determine the PPY-RGO coated wood with the optimal PPY-RGO ratio that yielded the highest solar-to-vapor conversion efficiency.

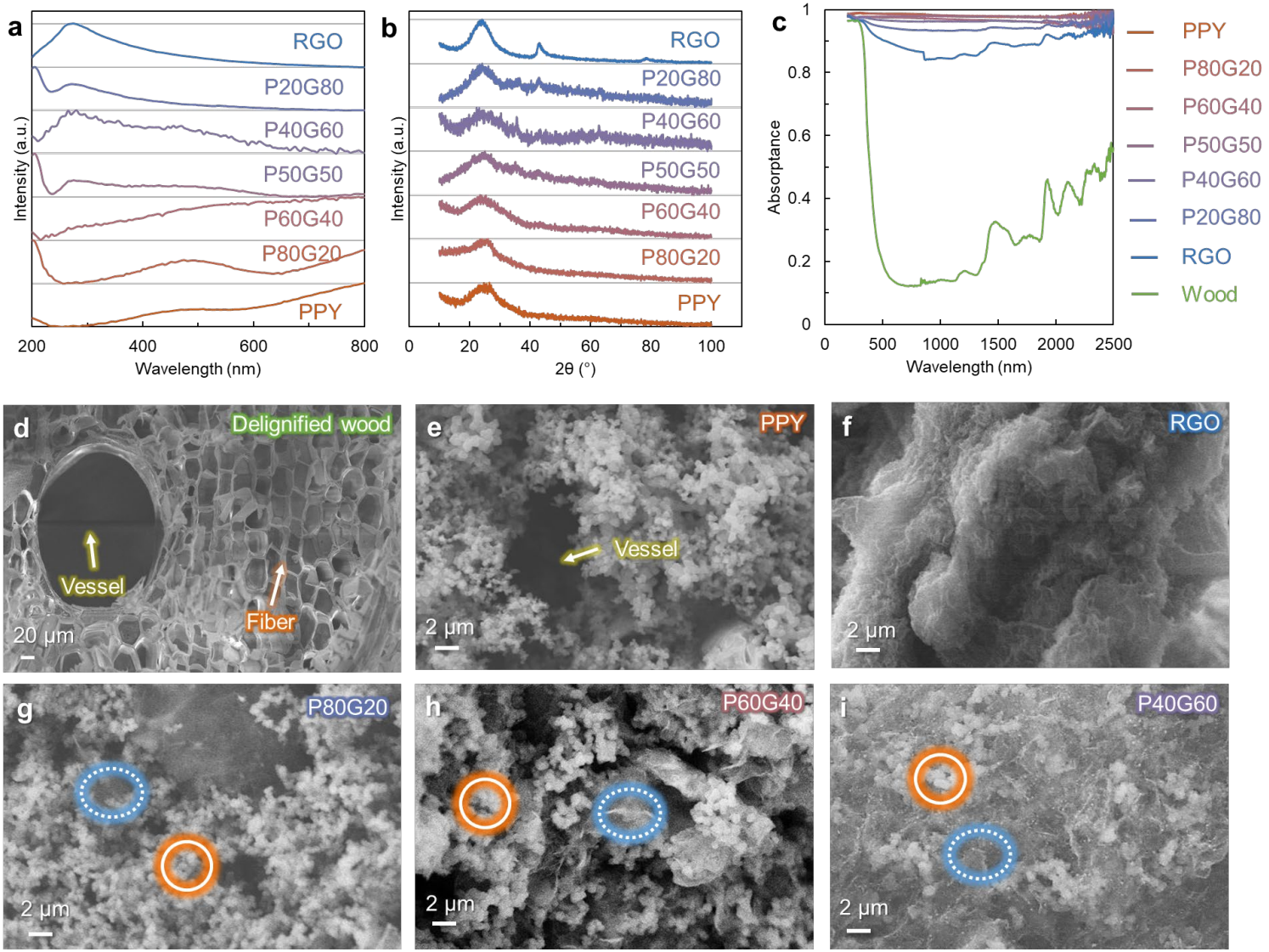
a
RGO
P20G80
P40G60
P50G50
P60G40
P80G20
PPY
Intensity (a.u.)
200
400
600
800
Wavelength (nm)
b
RGO
P20G80
P40G60
P50G50
P60G40
P80G20
PPY
Intensity (a.u.)
0
20
40
60
80
100
2θ (°)
c
Absorptance
0
0.2
0.4
0.6
0.8
1
0
500
1000
1500
2000
2500
Wavelength (nm)
PPY
P80G20
P60G40
P50G50
P40G60
P20G80
RGO
Wood
d
Delignified wood
Vessel
Fiber
20 μm
e
PPY
Vessel
2 μm
f
RGO
2 μm
g
P80G20
2 μm
h
P60G40
2 μm
i
P40G60
2 μm

Figure 2: (a) UV-VIS-NIR spectra and (b) XRD spectra of PPY-RGO samples with different mixing ratios, and (c) solar absorption spectra of the PPY-RGO coated wood with different mixing ratios. SEM images of (d) the delignified wood, and the PPY-RGO wood with different mixing ratios, namely (e) 100:0 (PPY), (f) 0:100 (RGO), (g) 80:20, (h) 60:40, (i) 40:60. The orange and blue circles in (g) and (h) indicate the PPY powder and RGO layer on the wood surface.

4.2. Surface profile

The surface profiles of the delignified wood, the woods coated by PPY, PPY-RGO composite materials, and RGO are shown in Figures 2(d) – (i). It is noted that the delignified Balsa wood is composed of vessels of about 200 μm in size and fibers of 20-50 μm in size. The fibers can facilitate water diffusion during the capillary effect so that the evaporated area of the wood surface can be re-wet quickly. Moreover, a study indicated that a channel with a larger diameter can help remove the salt from the wood surface [13]. As a result, the PPY-RGO coated wood can also be used for desalination. From the SEM image, it can be seen that the PPY powder formed a nanoscale porous layer on the wood surface, covering the micro-scale channel on the wood surface. The PPY porous structure not only can support light scattering, increasing solar absorption but also facilitates the water spread on the coating layer through the capillary effect. On the other hand, the RGO coating shrinks into particle form as shown in Figure 1(a) due to the restacking of RGO layers. The RGO layer stacking is caused by the π-π interaction [49]. From the SEM image of the RGO powder on the wood surface, the RGO layers are accumulated together. Due to the non-porous structure of the RGO layer, the RGO structure cannot improve solar absorption through light scattering. Therefore, the solar absorptance of the RGO coated wood is the lowest. By comparing the SEM images of P80G20, P60G40, and P40G60 woods, it is clear that reducing the PPY content can reduce the proportion of the PPY porous structure on the coated wood. Moreover, although the area of the PPY porous structure is reduced when the PPY content is decreased, the presence of the RGO layer connects the PPY powders. As a result, the heat transfer across the PPY particles can be improved. In addition, the restacking of the RGO layer is suppressed based on the SEM images because of the anchoring of the pyrrole monomer on the RGO surface. Therefore, the area of solar absorption can be maintained to ensure sufficient solar input for evaporation. The solar absorption spectrum of the PPY-RGO coated wood also confirms that the solar absorption of the PPY-RGO coated wood is close to 98% due to the suppression of RGO restacking by the presence of PPY particles. The solar absorption performance of the PPY-RGO coated wood is improved

by 10.9% compared to the RGO coated wood. Consequently, the PPY-RGO coated wood with improved solar absorption and heat transfer performance is obtained.

4.3. Thermal property

As mentioned above, apart from solar absorption, the photothermal conversion performance of the interfacial steam generator is also important for water evaporation. The photothermal conversion performance of the coated wood can be evaluated by the temperature change and the maximum surface temperature of the wood and coated wood under one sun (1000 $W \cdot m^{-2}$) as presented in Figures 3(a) and (b). The heat localization on the coated wood surfaces can also be observed from the thermal images in Figure 3(b). Under solar irradiance, the temperature of the samples rises rapidly in the first two to three minutes. The surface temperatures of the samples are relatively constant after 15 minutes. The surface temperature of the coated woods is greater than that of the wood without coating due to the enhanced solar absorptance. It is observed that the surface temperature of the PPY-RGO coated wood increases with the RGO content, reaching the maximum (50.3 ^{o}C) when the RGO content is 40%. Then, the surface temperature of the PPY-RGO coated wood decreases slightly as the RGO content increases. The improved surface temperature of the PPY-RGO coated wood may be due to the PPY deposited RGO layer. The RGO structure can be treated as the conductive network of the PPY. Due to the reduced phonon mean free path between the PPY powders, PPY powder can disperse heat to the surrounding efficiently after absorbing sunlight [50]. Therefore, the photothermal conversion efficiency of the PPY-RGO coated wood is improved. The improved heat transfer of the PPY-RGO coating can thus lead to a higher surface temperature of the coated wood under sunlight even though the solar absorption performance is lower. On the other hand, when the RGO content increases, the restacking of the PPY-RGO coating becomes more significant, so the cracking of the PPY-RGO coating leads to the reduction of the coated surface. The disconnected coated surface resists the heat transfer between the PPY powders, reducing the efficiency of heat transfer along the coated surface. Therefore, the heat dissipation of the PPY-RGO to the surrounding air may be increased. The reduction of PPY (high solar absorptance) content is also one of the reasons for the decreasing surface temperature trend of the PPY-RGO coated wood.

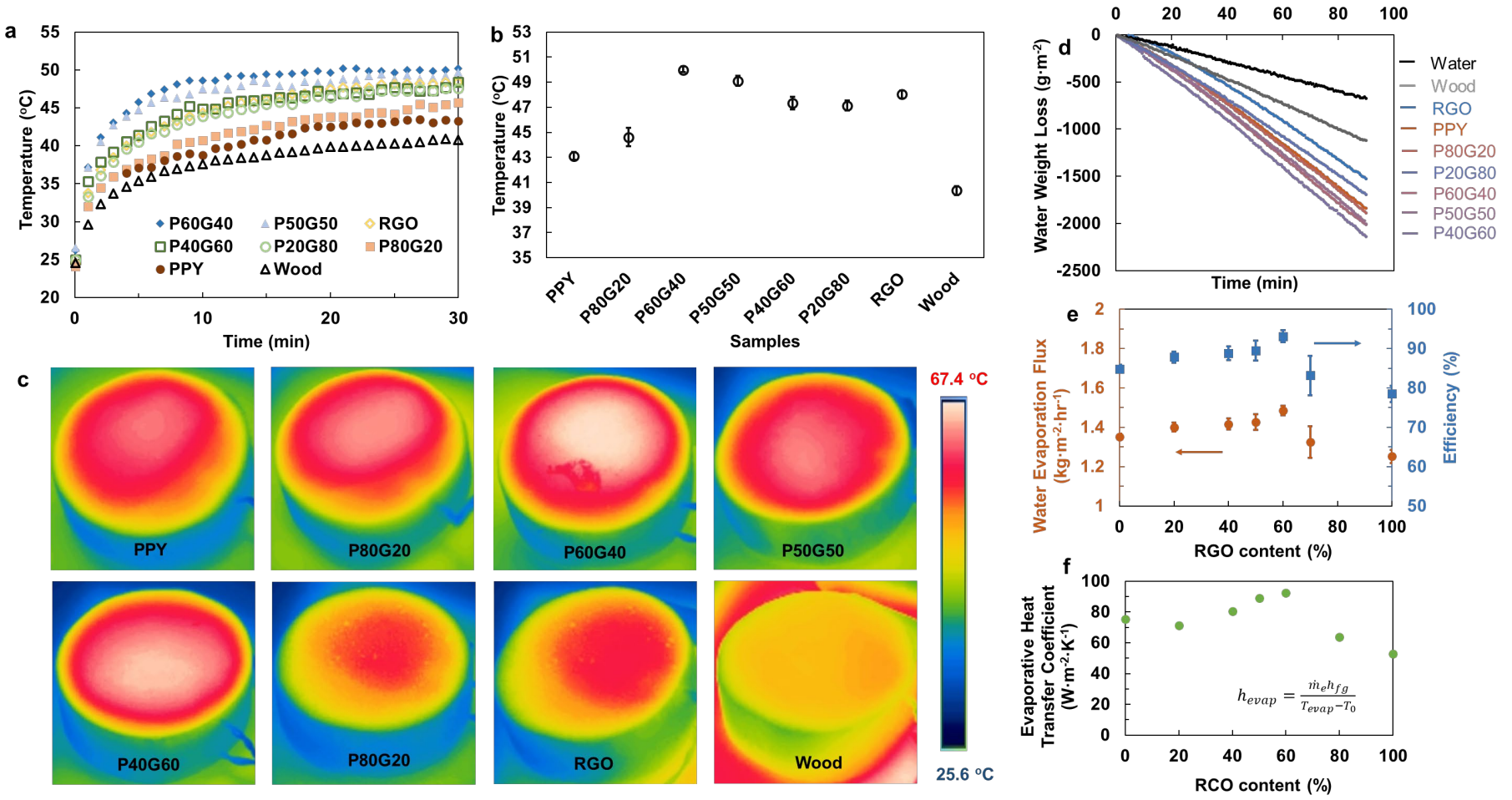
a
Temperature (°C)
Time (min)
P60G40
P50G50
RGO
P40G60
P20G80
P80G20
PPY
Wood
b
Temperature (°C)
PPY
P80G20
P60G40
P50G50
P40G60
P20G80
RGO
Wood
Samples
c
PPY
P80G20
P60G40
P50G50
P40G60
P80G20
RGO
Wood
67.4 °C
25.6 °C
d
Water Weight Loss (g·m⁻²)
Time (min)
Water
Wood
RGO
PPY
P80G20
P20G80
P60G40
P50G50
P40G60
e
Water Evaporation Flux (kg·m⁻²·hr⁻¹)
Efficiency (%)
RGO content (%)
f
Evaporative Heat Transfer Coefficient (W·m⁻²·K⁻¹)
$h_{evap} = \frac{\dot{m}_e h_{fg}}{T_{evap} - T_0}$
RCO content (%)

Figure 3: (a) Temperature change of the dry PPY-RGO coated wood under one sun, (b) the maximum temperature of the dry PPY-RGO coated wood under one sun and the thermal images of the PPY-RGO coated woods under light illumination, (c) water weight reduction of different PPY-RGO coated woods during the water evaporation test, (d) water evaporation fluxes and solar-vapor conversion efficiencies of PPY-RGO coated woods with various RGO contents, and (e) the evaporative heat transfer coefficients of different PPY-RGO coated woods.

4.4. Evaporation performance

The weight loss of water evaporated during the evaporation test under one sun is shown in Figure 3(d). It is noted that the weight reduction of the water is relatively linear for all samples. Among the coated wood samples, the water weight reduction is the highest when using P40G60 coated wood as the evaporator while the RGO coated wood causes the lowest water mass reduction. Nevertheless, the water mass reduction of RGO coated wood is 125.9% and 38.1% higher than that of pure water and wood, respectively. This indicates that coating photothermal materials on the wood surface can improve the water evaporation rate due to enhanced solar absorptance and heat localization. The water evaporation rates of various coated wood samples are determined by Equation (2), and the results are shown in Figure 3(e). The water evaporation rate of the coated wood was firstly increased by the RGO content reaching the maximum with an RGO content of 40%. While the RGO content is higher than 60%, the water evaporation rate of the coated wood sample decreased relatively sharply. Since the water evaporation rates of the samples were not steady at the beginning of the evaporation test, the water evaporation rates presented were calculated based on the water weight loss during the last 30 minutes. Among them, the P40G60 coated wood yielded the highest water evaporation flux and solar-vapor conversion efficiency of 1.49 $kg \cdot m^{-2} \cdot hr^{-1}$ (1.49 $L \cdot kWh^{-1}$ under 1000 $W \cdot m^{-2}$) and 93.1%, respectively. As compared to the PPY and RGO coated wood, the water evaporation performance of P40G60 coated wood was enhanced by 9.8% and 18.6%, respectively. The average variation of the measured water evaporation rates is about 2.55%. The evaporation heat transfer coefficients as shown in Figure 3(f) also indicate that the water evaporation performance of the PPY-RGO coated wood is more efficient when the RGO content increases to 60%. Then, the further addition of the RGO content decreases the evaporation efficiency of the PPY-RGO coated woods. The enhanced water evaporation performance of PPY-RGO coated wood compared to PPY and RGO coated wood indicates the synergistic effect of PPY and RGO on water evaporation improvement. The factors affecting the water evaporation performances of the PPY-RGO coated wood include solar absorptance, the heat transfer

network of the PPY-RGO coating, and the molecular interaction between the PPY-RGO coating and the water molecules. As discussed in section 4.1, the solar absorptance of PPY coated wood is higher than RGO and the addition of RGO can lead to a reduction in the solar absorptance of the PPY-RGO coated wood. Therefore, when the RGO content is higher, less solar energy is absorbed by the coated wood for evaporation. Therefore, it is expected that the decreasing trend of the evaporation rate in Figure 3(e) is caused by the low solar absorptance of the coated wood. Nonetheless, the increasing trend of the water evaporation rate in Figure 3(e) further indicates that the addition of RGO can improve the water evaporation rate. The molecular dynamics simulations from Zhang et al. [51] proved that hydrophilic functional groups (-OH) on RGO can improve water evaporation due to the interactions of the -OH groups with the surrounding water molecules. In addition, based on the SEM images (Figures 2(g) and (h)), the 2D RGO layer helps to connect the PPY porous structure. Therefore, the heat transfer between the PPY porous structure is more efficient for the PPY-RGO coating. The trade-off between solar energy absorption and water evaporation improvement leads to an optimum weight ratio between the PPY and RGO (PPY:RGO = 40:60) for solar-to-vapor conversion efficiency. The water evaporation performance of the P40G60 wood under 2 suns was also investigated and is shown in Figure 4(c). It was noted that the solar-to-vapor conversion efficiency of the P40G60 wood (91.3% at 2 suns) was reduced with the increased solar intensity. Similar results have also been shown in the previous study [5]. The reason behind this is the increase in the convective and radiative heat loss due to the rise in the evaporation surface temperature of the coated wood. To investigate the potential of the proposed PPY-RGO coated woods in desalination applications, the solar-to-vapor conversion efficiency of the P40G60 coated woods submerged in saline water (3.5% of salt) was measured. The evaporation test of the P40G60 coated wood (highest water evaporation performance) using saline water (3.5% salt, similar to seawater) was conducted to investigate the performance of the proposed PPY-RGO coated under a high salinity environment. From Figure S1 in the supporting information, although the efficiency of the PPY-RGO coated wood was reduced slightly while placed in saline water, the evaporation performance of the coated wood can be maintained for more than 3 hours. Besides, the photos in Figure S1(b) indicate that the visible salt formation on the coated wood appeared after evaporation for over 130 minutes, while the salt crystal disappeared after 52 minutes when the solar simulator was off. Therefore, it is expected that the PPY-RGO coated wood can be applied in solar desalination systems with stable evaporation performance. When comparing the PPY-RGO coated wood in this work with other wood-based interfacial

steam generators in the literature, it should be highlighted that the PPY-RGO coated wood in this study shows supreme solar-to-vapor conversion efficiency as shown in Figure 4.

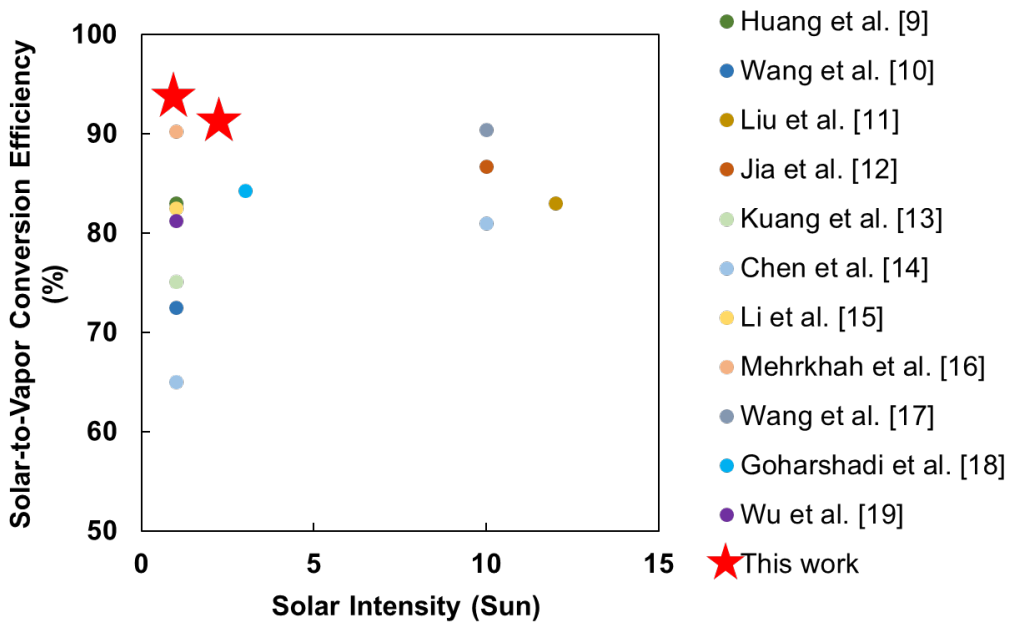

Figure 4: Comparison of the solar-to-vapor conversion efficiency of the fabricated PPY-RGO coated wood with different wood-based interfacial steam generators in the literature [9–19].

4.5. Transient heat transfer analysis of the PPY-RGO coated wood

There is a big research gap in the analysis of transient heat transfer on the evaporation performance of the interfacial steam generator. Thus, mathematical models have been developed in this study to investigate the transient heat transfer mechanism of the PPY-RGO coated wood during evaporation. The water evaporation rates of the coated woods could be anticipated using Equation (7) together with the coated wood temperatures measured during the evaporation. The coefficient A was determined by best-fit principles. The resulting coefficient A and the corresponding SSE (Equation 8) are listed in Table 2. The comparison between the experimental and calculated water evaporation rates (based on Equation (7)) of different coated wood samples is presented in Figures 5(a) – (g). The modeling results are well-matched to the experimental results, indicating that the water evaporation of the coated wood depends on the vapor pressure difference between the saturated coated wood surface and the surrounding air. As a result, when the humidity of the surrounding air is lower, the water evaporation performance of the coated wood can be improved. To further understand the effect of the surface temperature of the coated wood and the surrounding air temperature on the water

evaporation performance of the coated wood, heat loss analysis of P40G60 coated wood, which yielded the highest water evaporation and solar-to-vapor conversion efficiency, was conducted. The conductive, convective, and radiative heat losses of P40G60 coated wood were determined based on Equations (9) – (11) and the measured temperatures of the coated wood and surrounding air during the evaporation test. From Figure 5(h), it is noted that the conductive heat loss is significant at the beginning of the evaporation test, accounting for 21.9% of the total energy. As time passed, the effect of conductive heat loss was reduced and reached zero after 30 minutes. This is because the temperature of the coated wood became uniform in the vertical direction after the initial state. On the other hand, it was observed that the convective heat loss and radiative heat loss increased with time during the evaporation test. According to Equations (9) and (11), the convective and radiative heat loss can be raised by the difference between the coated wood surface temperature and the surrounding temperature. Therefore, decreasing the wood surface temperature by modifying the wood structure can improve the evaporation performance of the samples. However, it should also be noted that although minimizing the temperature difference between the coated wood sample and the surrounding can reduce the heat loss of the coated wood, the impact of relative humidity of the surrounding becomes more significant in this condition according to Equation (7). In addition, the removal of the evaporated vapor accumulated near the evaporation surface will be reduced due to the reduced buoyancy-driven air movement.

Table 2: The coefficient A for Equation (7) and corresponding SSE from Equation (8) of different PPY-RGO coated woods

Samples	A	SSE
PPY coated wood	2.19	0.0422
P80G20 coated wood	2.10	0.0439
P60G40 coated wood	2.37	0.0608
P50G50 coated wood	2.49	0.0578
P40G60 coated wood	2.54	0.195
P20G80 coated wood	1.89	0.00775
RGO coated wood	1.58	0.0970

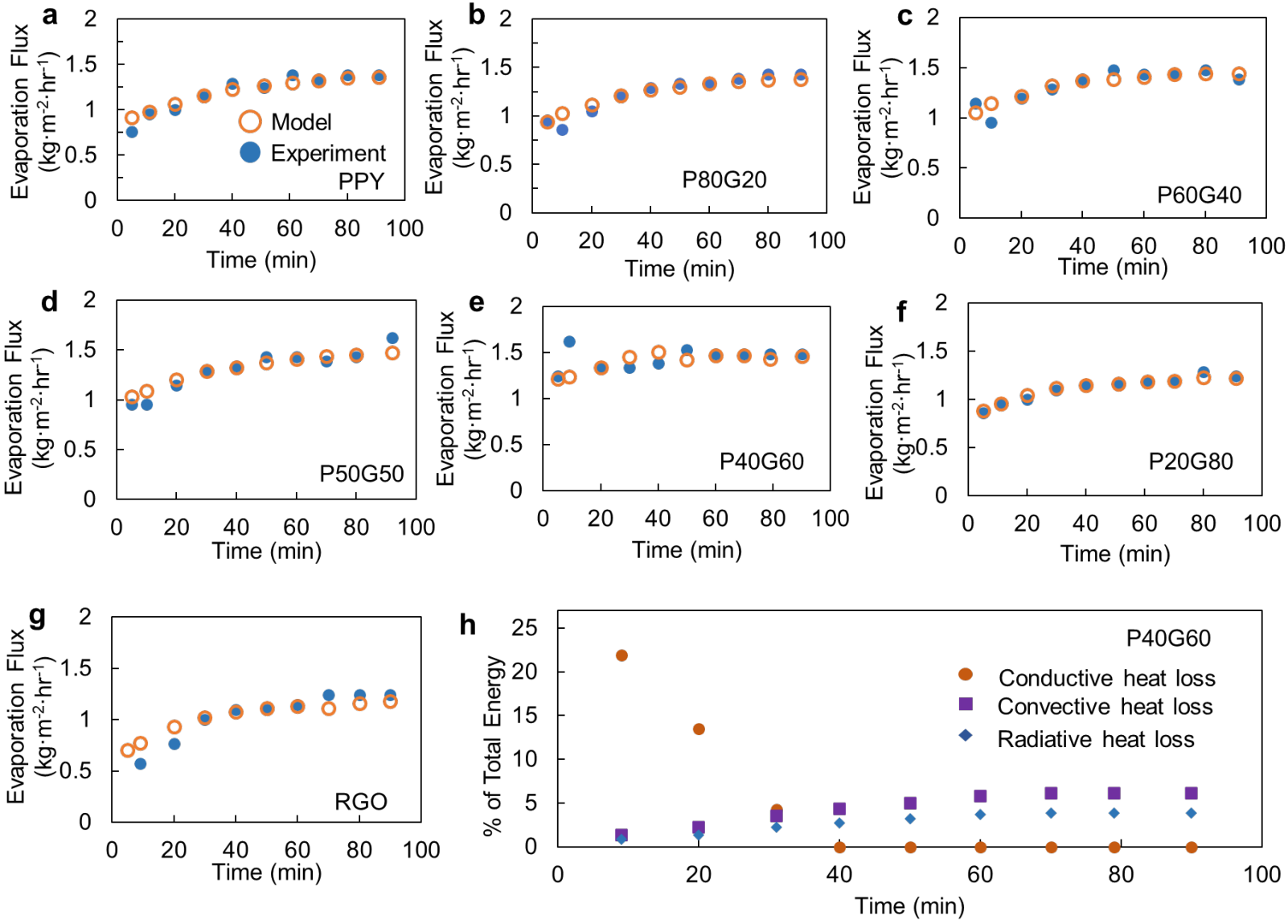
a
b
c
d
e
f
g
h
Evaporation Flux
(kg·m-2·hr-1)
Time (min)
Model
Experiment
PPY
P80G20
P60G40
P50G50
P40G60
P20G80
RGO
% of Total Energy
Conductive heat loss
Convective heat loss
Radiative heat loss

Figure 5: The transient modelling and experimental water evaporation fluxes of PPY-RGO coated woods with PPY-RGO ratios of (a) 100:0 (PPY), (b) 80:20, (c) 60:40, (d) 50:50, (e) 40:60, (f) 20:80, and (g) 0:100 (RGO). (h) The conductive, convective, and radiative heat losses of P40G60 coated wood during the evaporation test.

5. Conclusion

While water evaporation is one of the main processes in various thermal systems, investigating a highly-efficient solar-driven interfacial steam generator can improve the efficiency of different thermal systems. Inspired by the transpiration in plants, polypyrrole-reduced graphene oxide coated woods were fabricated and investigated in this study. With the naturally developed water supply pathway of the wood substrate, the high solar absorption of polypyrrole, and the reduced graphene oxide constructed heat transfer pathway, the polypyrrole-reduced graphene oxide coated wood showed a supreme water evaporation rate and solar-vapor conversion efficiency compared to polypyrrole or reduced graphene oxide coated woods. The highest water evaporation flux (1.49 $kg \cdot m^{-2} \cdot hr^{-1}$) and solar-vapor conversion efficiency (93.1%) were obtained by P40G60 coated wood, showing 9.8% and 18.6% improvement as compared to that of polypyrrole and reduced graphene oxide coated wood, respectively. More importantly, the solar-to-vapor conversion efficiency of the polypyrrole-reduced graphene oxide coated wood was above most of the wood-based interfacial steam generators in the literature. Mathematical models were also firstly proposed to investigate the transient heat transfer and evaporation performances of the polypyrrole-reduced graphene oxide coated wood. The results confirmed that the water evaporation performance of the coated wood depended on the vapor pressure difference between the evaporation surface and the surrounding air. Moreover, the polypyrrole-reduced graphene oxide coated wood was significantly affected by the downward conductive heat loss only at the initial stage of the evaporation process, while under the steady-state, the water evaporation performance of the coated wood was mainly influenced by the convective heat loss, followed by the radiative heat loss. By investigating the transient water evaporation and heat transfer performances of the polypyrrole-reduced graphene oxide coated wood, it is believed that this study not only can provide the guidelines for future study and application of the coated wood in water evaporation systems but also encourage the application of interfacial steam generation in various thermal systems to enhance efficiency.

CRediT authorship contribution statement

Man Yi Wong: Conceptualization, Methodology, Formal analysis, Investigation, Writing - original draft, Visualization. **Yihao Zhu:** Visualization, Writing - review & editing. **Tsz Chung Ho:** Methodology, Investigation, Writing - review & editing. **Aiqiang Pan:** Methodology, Formal analysis, Writing - original draft. **Chi Yan Tso:** Conceptualization, Methodology, Resource, Supervision, Writing - review & editing, Project administration, Funding acquisition.

Acknowledgments

The funding for this research is provided by the Hong Kong Research Grant Council (RGC) via Early Career Scheme (ECS) account 21200819 and General Research Fund (GRF) account 11200121.

Declaration of Competing Interest

The authors declare that they have no known competing financial interests or personal relationships that could have appeared to influence the work reported in this paper.

References

[1] Sheng, M., Yang, Y., Bin, X., Zhao, S., Pan, C., Nawaz, F., et al. (2021) Recent advanced self-propelling salt-blocking technologies for passive solar-driven interfacial evaporation desalination systems. *Nano Energy*. 89 (PB), 106468.

[2] Xie, Z., Peng, Y.P., Yu, L., Xing, C., Qiu, M., Hu, J., et al. (2020) Solar-Inspired Water Purification Based on Emerging 2D Materials: Status and Challenges. *Solar RRL*. 4 (3), 1900400.

[3] Chang, C., Tao, P., Xu, J., Fu, B., Song, C., Wu, J., et al. (2019) High-Efficiency Superheated Steam Generation for Portable Sterilization under Ambient Pressure and Low Solar Flux. *ACS Applied Materials and Interfaces*. 11 (20), 18466–18474.

[4] Liu, G., Chen, T., Xu, J., Li, G., and Wang, K. (2020) Solar evaporation for simultaneous steam and power generation. *Journal of Materials Chemistry A*. 8 (2), 513–531.

[5] Tao, P., Ni, G., Song, C., Shang, W., Wu, J., Zhu, J., et al. (2018) Solar-driven interfacial evaporation. *Nature Energy*. 3 (12), 1031–1041.

[6] Wang, Z., Liu, Y., Tao, P., Shen, Q., Yi, N., Zhang, F., et al. (2014) Bio-inspired evaporation through plasmonic film of nanoparticles at the air-water interface. *Small*. 10 (16), 3234–3239.

[7] Li, J., Du, M., Lv, G., Zhou, L., Li, X., Bertoluzzi, L., et al. (2018) Interfacial Solar Steam Generation Enables Fast-Responsive, Energy-Efficient, and Low-Cost Off-Grid Sterilization. *Advanced Materials*. 30 (49), 1805159.

[8] Min, X., Zhu, B., Li, B., Li, J., and Zhu, J. (2021) Interfacial Solar Vapor Generation : Materials and Structural Design. *Acc.Mater.Res*. 2021 (1),.

[9] Huang, W., Hu, G., Tian, C., Wang, X., Tu, J., Cao, Y., et al. (2019) Nature-inspired salt resistant polypyrrole-wood for highly efficient solar steam generation. *Sustainable Energy and Fuels*. 3 (11), 3000–3008.

[10] Wang, Z., Yan, Y., Shen, X., Jin, C., Sun, Q., and Li, H. (2019) A wood-polypyrrole composite as a photothermal conversion device for solar evaporation enhancement. *Journal of Materials Chemistry A*. 7 (36), 20706–20712.

[11] Liu, K.K., Jiang, Q., Tadepalli, S., Raliya, R., Biswas, P., Naik, R.R., et al. (2017) Wood-Graphene Oxide Composite for Highly Efficient Solar Steam Generation and Desalination. *ACS Applied Materials and Interfaces*. 9 (8), 7675–7681.

[12] Jia, C., Li, Y., Yang, Z., Chen, G., Yao, Y., Jiang, F., et al. (2017) Rich Mesostructures Derived from Natural Woods for Solar Steam Generation. *Joule*. 1 (3), 588–599.

[13] Kuang, Y., Chen, C., He, S., Hitz, E.M., Wang, Y., Gan, W., et al. (2019) A High-Performance Self-Regenerating Solar Evaporator for Continuous Water Desalination. *Advanced Materials*. 31 (23), 1900498.

[14] Chen, C., Li, Y., Song, J., Yang, Z., Kuang, Y., Hitz, E., et al. (2017) Highly Flexible and Efficient Solar Steam Generation Device. *Advanced Materials*. 29 (30), 1701756.

[15] Li, Z., Zheng, M., Wei, N., Lin, Y., Chu, W., Xu, R., et al. (2020) Broadband-absorbing WO3-x nanorod-decorated wood evaporator for highly efficient solar-driven interfacial steam generation. *Solar Energy Materials and Solar Cells*. 205 (July 2019), 110254.

[16] Mehrkhah, R., Goharshadi, E.K., Ghafurian, M.M., Mohammadi, M., and Mahian, O. (2021) Clean water production by non-noble metal/reduced graphene oxide nanocomposite coated on wood: Scalable interfacial solar steam generation and heavy metal sorption. *Solar Energy*. 224 (November 2020), 440–454.

[17] Wang, M., Wang, P., Zhang, J., Li, C., and Jin, Y. (2019) A Ternary Pt/Au/TiO 2 -Decorated Plasmonic Wood Carbon for High-Efficiency Interfacial Solar Steam Generation and Photodegradation of Tetracycline. *ChemSusChem*. 12 (2), 467–472.

[18] Goharshadi, K., Sajjadi, S.A., Goharshadi, E.K., and Mehrkhah, R. (2022) Highly

efficient plasmonic wood/Ag/Pd photoabsorber in interfacial solar steam generation. *Materials Research Bulletin*. 154 (March), 111916.

[19] Wu, D., Gao, Y., Dai, Z., Chen, B., Wang, C., and Zhang, X. (2022) Alkali treatment combined with surface carbonized wood for high-efficiency solar interfacial evaporation. *Applied Thermal Engineering*. 213 (March), 118646.

[20] Cao, S., Rathi, P., Wu, X., Ghim, D., Jun, Y.S., and Singamaneni, S. (2020) Cellulose Nanomaterials in Interfacial Evaporators for Desalination: A "Natural" Choice. *Advanced Materials*. 2000922.

[21] Geng, Y., Jiao, K., Liu, X., Ying, P., Odunmbaku, O., Zhang, Y., et al. (2022) Applications of bio-derived/bio-inspired materials in the field of interfacial solar steam generation. *Nano Research*. 15 (4), 3122–3142.

[22] Boriskina, S. V., Ghasemi, H., and Chen, G. (2013) Plasmonic materials for energy: From physics to applications. *Materials Today*. 16 (10), 375–386.

[23] Zhu, L., Gao, M., Peh, C.K.N., and Ho, G.W. (2019) Recent progress in solar-driven interfacial water evaporation: Advanced designs and applications. *Nano Energy*. 57 507–518.

[24] Chen, C., Kuang, Y., and Hu, L. (2019) Challenges and Opportunities for Solar Evaporation. *Joule*. 3 (3), 683–718.

[25] Dao, V.-D. and Choi, H.-S. (2018) Carbon-Based Sunlight Absorbers in Solar-Driven Steam Generation Devices. *Global Challenges*. 2 (2), 1700094.

[26] Cheng, G., Wang, X., Liu, X., He, Y., and Balakin, B. V. (2019) Enhanced interfacial solar steam generation with composite reduced graphene oxide membrane. *Solar Energy*. 194 415–430.

[27] Zhuang, P., Fu, H., Xu, N., Li, B., Xu, J., and Zhou, L. (2020) Free-standing reduced graphene oxide (rGO) membrane for salt-rejecting solar desalination via size effect. *Nanophotonics*. 9 (15), 4601–4608.

[28] Xu, Y., Lin, Z., Zhong, X., Huang, X., Weiss, N.O., Huang, Y., et al. (2014) Holey graphene frameworks for highly efficient capacitive energy storage. *Nature Communications*. 5 4554.

[29] Ren, H., Tang, M., Guan, B., Wang, K., Yang, J., Wang, F., et al. (2017) Hierarchical Graphene Foam for Efficient Omnidirectional Solar–Thermal Energy Conversion. *Advanced Materials*. 29 (38), 1702590.

[30] Wang, M., Duan, X., Xu, Y., and Duan, X. (2016) Functional Three-Dimensional Graphene/Polymer Composites. *ACS Nano*. 10 (8), 7231–7247.

[31] Wang, X., Liu, Q., Wu, S., Xu, B., and Xu, H. (2019) Multilayer Polypyrrole Nanosheets with Self-Organized Surface Structures for Flexible and Efficient Solar–Thermal Energy Conversion. *Advanced Materials*. 31 (19), 1807716.

[32] Hao, D., Yang, Y., Xu, B., and Cai, Z. (2018) Efficient solar water vapor generation enabled by water-absorbing polypyrrole coated cotton fabric with enhanced heat localization. *Applied Thermal Engineering*. 141 406–412.

[33] Wen, B., Zhang, X., Yan, Y., Huang, Y., Lin, S., Zhu, Y., et al. (2021) Tailoring polypyrrole-based Janus aerogel for efficient and stable solar steam generation. *Desalination*. 516 (May), 115228.

[34] Bose, S., Kuila, T., Uddin, M.E., Kim, N.H., Lau, A.K.T., and Lee, J.H. (2010) In-situ synthesis and characterization of electrically conductive polypyrrole/graphene nanocomposites. *Polymer*. 51 (25), 5921–5928.

[35] Bose, S., Kim, N.H., Kuila, T., Lau, K.T., and Lee, J.H. (2011) Electrochemical performance of a graphene-polypyrrole nanocomposite as a supercapacitor electrode. *Nanotechnology*. 22 (36), 295202.

[36] Zaaba, N.I., Foo, K.L., Hashim, U., Tan, S.J., Liu, W.W., and Voon, C.H. (2017) Synthesis of Graphene Oxide using Modified Hummers Method: Solvent Influence. *Procedia Engineering*. 184 469–477.

[37] Borrega, M., Ahvenainen, P., Serimaa, R., and Gibson, L. (2015) Composition and structure of balsa (Ochroma pyramidale) wood. *Wood Science and Technology*. 49 (2), 403–420.

[38] Chen, Z., Dang, B., Luo, X., Li, W., Li, J., Yu, H., et al. (2019) Deep Eutectic Solvent-Assisted in Situ Wood Delignification: A Promising Strategy to Enhance the Efficiency of Wood-Based Solar Steam Generation Devices. *ACS Applied Materials and Interfaces*. 11 (29), 26032–26037.

[39] Skoog, D.A., Holler, F.J., and Crouch, S.R. (2007) Principles of instrumental analysis. 6th ed. Australia : Thomson Brooks/Cole, Australia.

[40] Shah, M.M. (2002) Evaluation of available correlations for rate of evaporation from undisturbed water pools to quiet air. *HVAC and R Research*. 8 (1), 125–131.

[41] Tang, R. and Etzion, Y. (2004) Comparative studies on the water evaporation rate from a wetted surface and that from a free water surface. *Building and Environment*. 39 (1), 77–86.

[42] Shah, M.M. (2022) Evaluation of methods for prediction of evaporation from water pools. *Journal of Building Physics*. 45 (5), 629–648.

[43] Çengel, Y.A. and Ghajar, A.J. (2015) Heat and mass transfer : fundamentals & applications. Fifth edit New York, N.Y. : McGraw-Hill Education, New York, N.Y.

[44] Ni, G., Li, G., Boriskina, S. V., Li, H., Yang, W., Zhang, T.J., et al. (2016) Steam generation under one sun enabled by a floating structure with thermal concentration. *Nature Energy*. 1 (9), 16126.

[45] Luo, X., Shi, J., Zhao, C., Luo, Z., Gu, X., and Bao, H. (2021) The energy efficiency of interfacial solar desalination. *Applied Energy*. 302 (August), 117581.

[46] Holman, J.P. (2010) Heat transfer. 10th ed. McGraw-Hill Higher Education, Mass, Boston.

[47] Bergman, T.L. and Incropera, F.P. (2011) Fundamentals of heat and mass transfer. 7th ed. / Hoboken, NJ : Wiley, Hoboken, NJ.

[48] Meng, D., Yang, S., Guo, L., Li, G., Ge, J., Huang, Y., et al. (2014) The enhanced photothermal effect of graphene/conjugated polymer composites: Photoinduced energy transfer and applications in photocontrolled switches. *Chemical Communications*. 50 (92), 14345–14348.

[49] Lee, J.H., Park, N., Kim, B.G., Jung, D.S., Im, K., Hur, J., et al. (2013) Restacking-inhibited 3D reduced graphene oxide for high performance supercapacitor electrodes. *ACS Nano*. 7 (10), 9366–9374.

[50] Aradhana, R., Mohanty, S., and Nayak, S.K. (2019) Synergistic effect of polypyrrole and reduced graphene oxide on mechanical, electrical and thermal properties of epoxy adhesives. *Polymer*. 166 (September 2018), 215–228.

[51] Zhang, M., Xu, F., Liu, W., Hou, Y., Su, L., Zhang, X., et al. (2022) Antibacterial evaporator based on reduced graphene oxide/polypyrrole aerogel for solar-driven desalination. *Nano Research*.

Supporting Information

Polypyrrole-Reduced Graphene Oxide Coated Delignified Wood for Highly Efficient Solar Interfacial Steam Generation

M.Y. Wong[1], Y. Zhu[1], T.C. Ho[1], A. Pan[1], C.Y. Tso[1,*]

[1] School of Energy and Environment, City University of Hong Kong, Hong Kong

* Corresponding Author Tel.: +852 3442 4623

E-mail address: chiytso@cityu.edu.hk

Address: School of Energy and Environment, City University of Hong Kong, Tat Chee Avenue, Kowloon, Hong Kong

Keywords: Evaporation, Solar Absorption, Photothermal Conversion, Heat Transfer, Solar-to-Vapor Conversion Efficiency

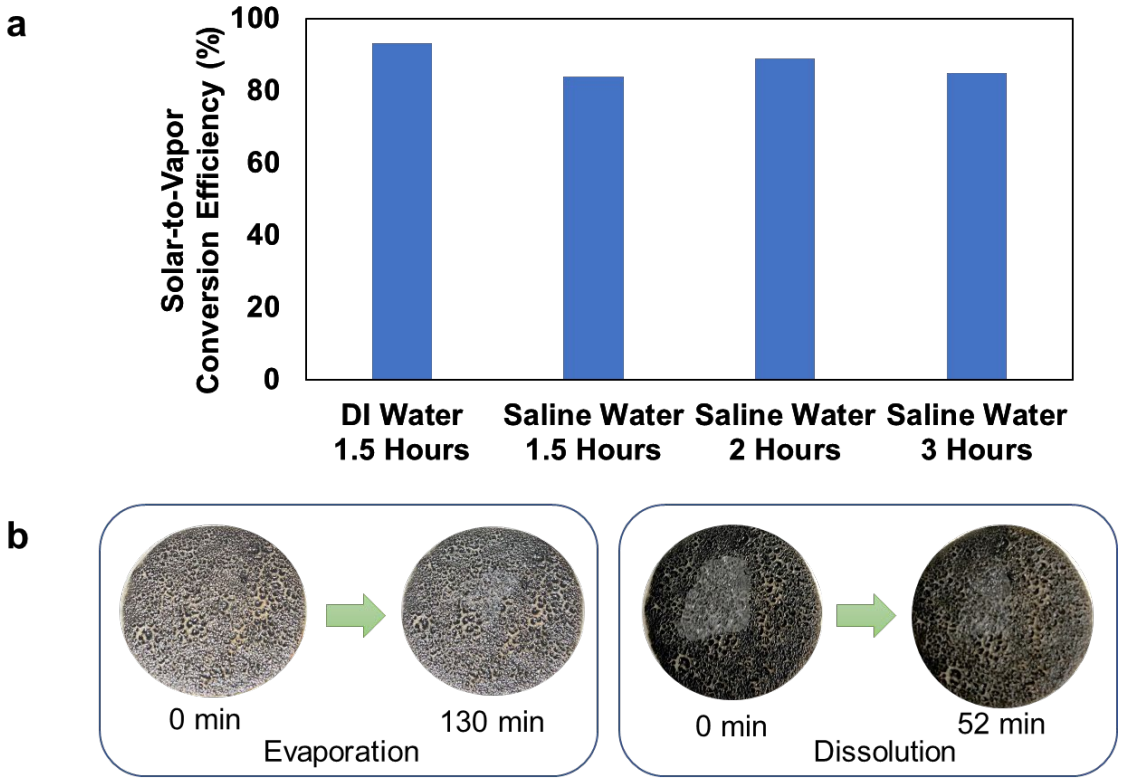

Figure S1: (a) The solar-to-vapor conversion efficiencies of the PPY-RGO coated woods in water and saline water, respectively, and (b) the photos of the salt formation and dissolution on PPY-RGO coated wood surface.